Passive Optical Sensing of the Near-Surface Wind-Driven Current Profile

NATHAN J. M. LAXAGUE, BRIAN K. HAUS, DAVID G. ORTIZ-SUSLOW, CONOR J. SMITH, GUILLAUME NOVELLI, HANJING DAI, TAMAY ÖZGÖKMEN, AND HANS C. GRABER

Department of Ocean Sciences, Rosenstiel School of Marine and Atmospheric Science, University of Miami, Miami, Florida

(Manuscript received 3 May 2016, in final form 31 March 2017)

ABSTRACT

Estimation of near-surface current is essential to the estimation of upper-ocean material transport. Wind forcing and wave motions are dominant in the near-surface layer [within $O(0.01)$ m of the surface], where the highly sheared flows can differ greatly from those at depth. This study presents a new method for remotely measuring the directional wind and wave drift current profile near to the surface (between 0.01 and 0.001 m for the laboratory and between 0.1 and 0.001 m for the field). This work follows the spectral analysis of high spatial ($\approx$0.002 m) and temporal resolution ($\approx$60 Hz) wave slope images, allowing for the evaluation of near-surface current characteristics without having to rely on instruments that may disturb the flow. Observations gathered in the 15 m $\times$ 1 m $\times$ 1 m wind-wave flume at the University of Miami's Surge-Structure-Atmosphere Interaction (SUSTAIN) facility show that currents retrieved via this method agree well with the drift velocity of camera-tracked dye. Application of this method to data collected in the mouth of the Columbia River (MCR) indicates the presence of a near-surface current component that departs considerably from the tidal flow and may be steered by the wind stress. These observations demonstrate that wind speed–based parameterizations alone may not be sufficient to estimate wind drift and to hold implications for the way in which surface material (e.g., debris or spilled oil) transport is estimated when atmospheric stress is of relatively high magnitude or is steered off the mean wind direction.

1. Introduction

The shape of the near-surface current profile has been the subject of scientific inquiry for many years—its direct effect on radar remote sensing (Goldstein et al. 1989) and oceanic material transport (Reed et al. 1994) have made defining its characteristics a worthy endeavor with far-reaching applications. The classic approach to estimating the direct effect of wind forcing on surface drift has been to parameterize the current as aligned with the wind velocity, with the magnitude given as a strict percentage of the 10-m neutral wind speed or friction velocity (e.g., Wu 1975). If one wishes to directly measure this near-surface drift, then it is essential to avoid disturbing the very flows that one is trying to observe, making remote sensing a strong candidate for this task. In the study of applied fluid mechanics, few phenomena are taken advantage of as frequently as the Doppler effect when observing moving and dynamic media. For example, the frequency shift in a backscattered radio or acoustic wave is measured and interpreted to produce the line-of-sight speed of the scatterer relative to the observer, allowing one to investigate the advection via current of particular wave components (e.g., Barrick et al. 1977; Plant and Wright 1980).

This strategy of Doppler current detection has been used extensively in the marine radar research community at gravity wave scales of $O(1–100)$ m, most notably by Young et al. (1985) and refined further by Senet et al. (2001). Generally speaking, the wavelength of a wave is directly proportional to the depth at which subsurface flows will advect it most strongly, with theoretical and empirical methods for extracting this proportionality provided in Stewart and Joy (1974) and Plant and Wright (1980). Advances in computer vision technology in recent years have allowed for the evaluation of the spatiotemporal characteristics that define the short high-frequency waves that are especially affected by near-surface current. A portion of Zappa et al. (2012) focused on the current-induced shift observed in the wavenumber–frequency spectra of high-resolution wave slope field time series (much like the present work). More recently, the

Denotes content that is immediately available upon publication as open access.

Corresponding author: Nathan J. M. Laxague, nlaxague@rsmas.miami.edu

DOI: 10.1175/JTECH-D-16-0090.1

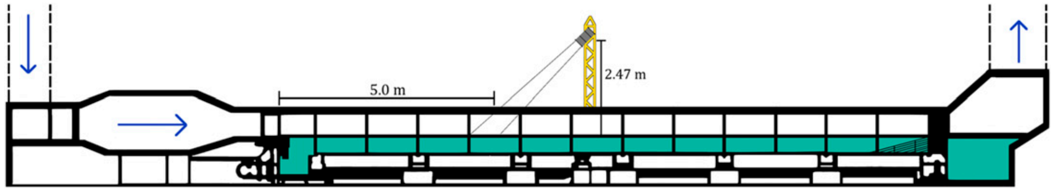

FIG. 1. Representation of ASIST wind-wave tank. The polarimetric camera was positioned 2.47 m above the mean water level and oriented 45° below the horizontal, with the footprint centered at 5-m fetch.

wavenumber–frequency spectral analysis performed on the stereophotogrammetric wave fields of Leckler et al. (2015) involved the currents affecting short gravity waves. Their work, though focused on the wave spectral properties in their own right, did extend the reach of this technique closer to the free surface through its improvement in spatial resolution.

There are a number of challenges associated with observing these short waves, not least of which is the possible contamination of the measurement from the instrument itself. Interpretation of electromagnetic radiation scattered from the water surface allows one to investigate a wide range of wave hydrodynamic phenomena without disrupting the air–sea interface (e.g., Hasselmann and Schieler 1970; Plant et al. 1999a). Furthermore, techniques that are able to retrieve synoptic spatial measurements of wave structure without disturbing the near-interfacial flows are ideal for the study of short ocean waves (e.g., Hara et al. 1994; Bock and Hara 1995). The polarimetric slope sensing (PSS) technique (Zappa et al. 2008) is an optical method designed to accomplish such a task; it has been successfully used to acquire short-scale wave structure from aboard a moving vessel (Laxague et al. 2015) and in a wind-wave tank (Laxague et al. 2017). The present study aims to take full advantage of this technology's high resolution in the recovery of near-surface wind-sensitive currents.

Observations were performed in both the Air–Sea Interaction Saltwater Tank (ASIST; see Fig. 1) at the University of Miami's Surge-Structure-Atmosphere Interaction (SUSTAIN) facility and the mouth of the Columbia River (MCR) along the Oregon–Washington border. For the laboratory observations, near-surface dye tracking was employed to provide a standard for Lagrangian fluid transport speed. For the field observations, the polarimetric camera was mounted off the starboard bow and oriented such that it imaged an area forward and away from the ship's wake zone. Two case studies were chosen, the first (MCR-1) corresponding to a flooding tide and the second (MCR-2) corresponding to an ebbing tide. Supporting long-wave and atmospheric stress measurements were made via a trio of ship-mounted acoustic altimeters and a sonic anemometer affixed to the bow mast, respectively.

In section 2a, the method for remote retrieval of short-wave slope fields and ensuing spectral analysis is described. The extraction of near-surface current from wavenumber frequency spectra is explained in section 2b. The particular implementation of these methods is split between the laboratory and field, with the results given in section 3. Section 4 contains a discussion of the results, and section 5 concludes the work.

2. Methods

a. Short-wave observation and spectral analysis

The analysis central to this work utilizes the PSS method. A complete description of the PSS method is contained within Zappa et al. (2008). The authors' execution of this method is explained in Laxague et al. (2015), with details specific to the MCR analysis given in Laxague et al. (2016) and details specific to laboratory analysis given in Laxague et al. (2017). Use of this optical system allows one to passively infer short-wave slope fields through the interpretation of their polarizing effect on reflected light (Zappa et al. 2008). In short, the method provides short-scale temporal and spatial information from waves without disturbing the near-interface flows that define them. The polarimeter used here is a FluxData FD-1665, a system enclosing a beamsplitter and three Basler Scout series charge-coupled devices (CCDs), each of which acquires images composed of visible light in one of the following three linear polarization states: 0°, 45°, and 90°. The lens used for this device is a Zeiss Distagon T* with a wide-angle lens and a focal length of 28 mm. Variations of the degree of linear polarization across the imaging footprint are processed to produce a slope field for each image triplet (Figs. 2a–c). For the field portion of the experiment, the camera was positioned such that it imaged an area of $\approx 1.56\,\mathrm{m}^2$ (yielding a wavenumber range of $5.00\,\mathrm{rad\,m}^{-1} < k < 1602\,\mathrm{rad\,m}^{-1}$). Each image was rectified according to the vessel's instantaneous linear accelerations and rotation rates as measured via the shipboard motion pack. The index of refraction for the air–sea interface is an important parameter in these calculations (Zappa et al. 2008), affecting the ultimate

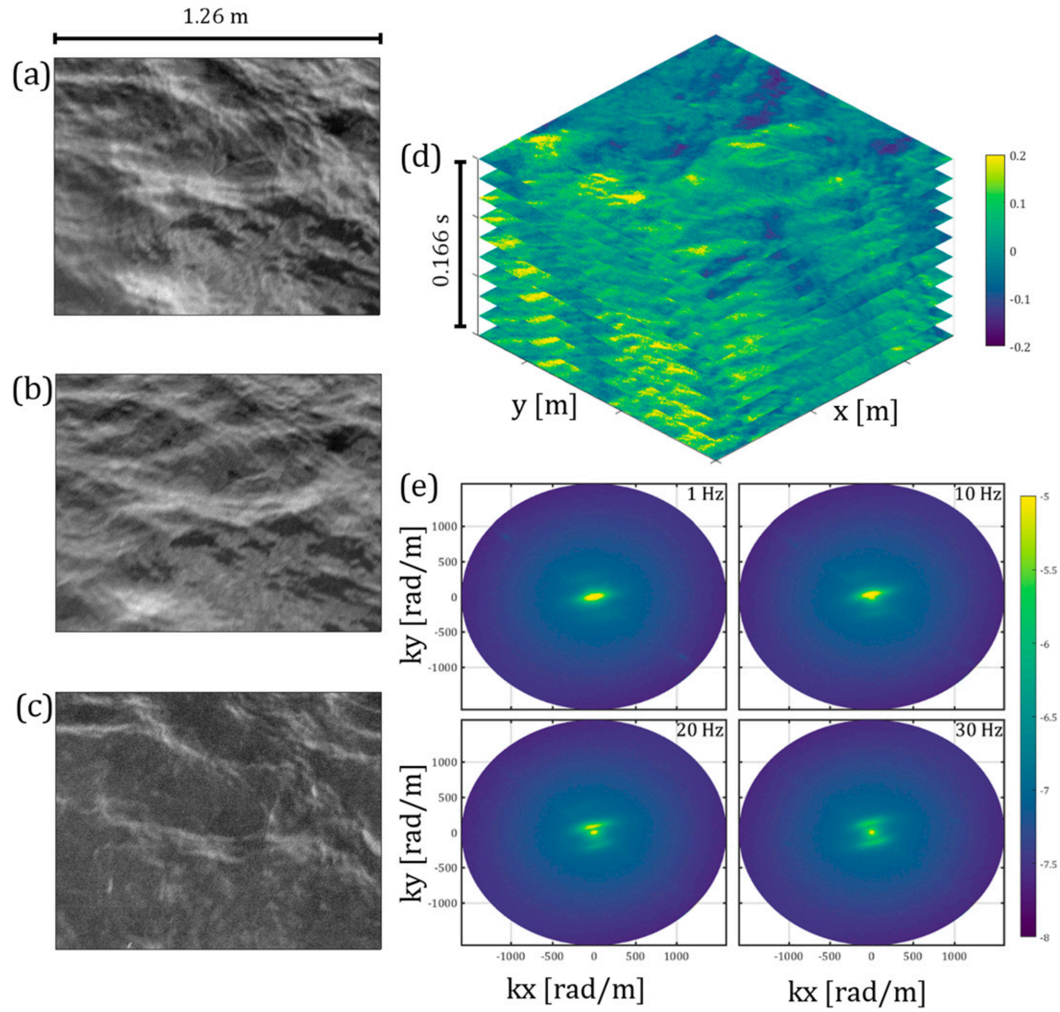

FIG. 2. Visual breakdown of the process from image triplet to $k-\omega$ spectrum. Raw image intensities in (a) 90°, (b) 45°, and (c) 0° polarizations. (d) Stack of slope fields forming $\mathbf{S}(x, y, t)$, colored by the wave slope magnitude in radians. (e) Four frequency slices from the resulting wavenumber–frequency spectrum $P(k_x, k_y, \omega)$, colored by the base-10 logarithm of directional wavenumber–frequency slope spectral density ($m^2\,Hz^{-1}\,rad^{-3}$).

magnitude of variations in the slope field. It should be noted that the index of refraction n was taken to be 1.33 for the field observations here. Application of the algorithm contained within Millard and Seaver (1990) to the R/V *Point Sur*'s flow-through water temperature and salinity measurements demonstrated that values should not have deviated more than 1% from this assumed value.

Each slope field was windowed with a two-dimensional Tukey (tapered cosine) window of tapering width $a = 0.2$. Once this was applied, each time series of slope field components (x, y) was gathered into three-dimensional slope field arrays $\mathbf{S}_x(x, y, t)$ and $\mathbf{S}_y(x, y, t)$, representing the spatiotemporal evolution of the wave slope field for analysis. It was convenient to account for the translational motion of the ship before applying the Fourier transform. This was accomplished by shifting each slice in space according to the displacement for that frame's time step, producing arrays $\mathbf{S}'_x(x, y, t)$ and $\mathbf{S}'_y(x, y, t)$, which are sheared in the direction of platform motion. The example slope field stack given in Fig. 2d shows no such shape; this is due to the negligible distance traveled by a ship proceeding at minimum steam over a 0.2-s interval. The resulting vector array was transformed into Fourier space,

$$g_x(k_x, k_y, \omega) = \int_0^T \int_0^Y \int_0^X e^{i(k_x x + k_y y - \omega t)} \mathbf{S}'_x(x, y, t)\, dx\, dy\, dt, \quad (1)$$

$$g_y(k_x, k_y, \omega) = \int_0^T \int_0^Y \int_0^X e^{i(k_x x + k_y y - \omega t)} \mathbf{S}'_y(x, y, t)\, dx\, dy\, dt. \quad (2)$$

In this description, x (k_x) and y (k_y) represent displacement (magnitude in wavenumber space); X and Y

are the corresponding length and width of the imaged area on the water surface, respectively; and T is the time over which the spectrum is computed. One may compute the three-dimensional wavenumber slope spectrum $P(k_x, k_y, \omega)$ (dimensions of $\mathrm{m^{-2}\,Hz^{-1}\,rad^{-3}}$) by multiplying the transformed function's magnitude by the appropriate constant,

$$P(k_x, k_y, \omega) = \frac{|g_x(k_x, k_y, \omega)|^2 + |g_y(k_x, k_y, \omega)|^2}{N k_{\max}^2 \omega_s}, \quad (3)$$

where N is the number of data points, $k_{\max} = \pi/\delta$, δ is the camera's spatial resolution (meters per pixel), $\omega_s = 2\pi f_s$, and f_s is the camera's frame rate (Hz). If the observational platform were to move such that the final frame had no spatial overlap with the first frame, then the resulting Fourier transform would not have been able to retain the wave phase information. However, for the purposes of the wavenumber–frequency analysis that follows, phase information does not factor into the desired product (wave-advecting near-surface current) when averaged over many waves. Only the spectral energy density in wavenumber and frequency are needed, allowing the work that follows to be performed from moving platforms with a wide range of averaging and processing window lengths. Because of computer RAM constraints, fast Fourier transform (FFT) processing window lengths were limited to 5 s. The variance resulting from these short FFT lengths has been minimized through the averaging of sequential spectra over a longer period of time—in this case, 5 min. The wavenumber–frequency spectra shown here (e.g., Fig. 2e) are representative of this averaging.

b. *The Doppler shift: Waves advected by currents*

The well-known Doppler effect plays an important role in the observation of ocean surface waves; specifically, a steady flow aligned with (opposed to) a particular wave's propagation direction will increase (decrease) its apparent frequency. The simultaneous recording of a wave's spatial and temporal characteristics will therefore grant an observer the ability to estimate the magnitude and direction of the currents that advect it.

The basis of this analysis rests on linear wave theory, in which one expects that an ocean wave system's peak energy should coincide with the curve defined by the deep-water gravity–capillary linear dispersion relation

$$\omega^2 = gk + \frac{\sigma}{\rho} k^3. \quad (4)$$

For the work performed here, g was taken to be $9.81\,\mathrm{m\,s^{-2}}$, σ was taken to be $0.07\,\mathrm{N\,m^{-1}}$ (Harkins and Brown 1919), and ρ was taken to be $\approx 1030\,\mathrm{kg\,m^{-3}}$, computed from the seawater equation of state given in Millero and Poisson (1981). Surfactants were assumed to play a negligible role in these estimates based on visual inspection of the sea surface and the shape of the capillary regime in the wavenumber spectra. For the range of temperatures and salinities measured via shipboard flow-through sensors, the value of σ was estimated to deviate no more than $0.01\,\mathrm{N\,m^{-1}}$ from its assumed value. This deviation was computed to yield no more than a $0.01\,\mathrm{m\,s^{-1}}$ bias in the current estimate due to the dominance of gravity as a restoring force for the waves analyzed here.

For a given wave with wavenumber k, the velocity of encounter $\mathbf{U}_E(k)$ represents the mean current that is felt by that wave component (Stewart and Joy 1974; Senet et al. 2001). The change to the deep-water gravity–capillary dispersion relation given an encounter current of $\mathbf{U}_E(k)$ (with directional difference between the wave propagation direction vector and the current vector called $\boldsymbol{\theta}$), an observed frequency of ω, and an intrinsic frequency of Ω is as follows:

$$\Omega^2 = gk + \frac{\sigma}{\rho} k^3, \quad (5)$$

$$\Omega^2 = (\omega - \mathbf{k} \cdot \mathbf{U}_E)^2, \quad (6)$$

$$\Omega = \omega - kU_E \cos(\theta). \quad (7)$$

It is convenient to divide both sides of Eq. (7) by k to isolate $U_E \cos(\theta)$ as the difference between the observed wave celerity c_p and intrinsic wave celerity c_0 as follows:

$$\frac{1}{k}[\omega - kU_E \cos(\theta)] = \frac{\Omega}{k}, \quad (8)$$

$$c_p - U_E \cos(\theta) = c_0, \quad (9)$$

$$c_p - c_0 = U_E \cos(\theta). \quad (10)$$

For a given ω (and given the encounter current), the quantity $U_E \cos(\theta)$ will have a maximum in the current direction. By noting the direction in which the dispersion shell is shifted, this angle is extracted [specifically, the coordinates (k_x, k_y) for which $U_E \cos(\theta)$ is maximum are identified]. The result of this process, given that the values of g, σ, and ρ are known (or may assumed to take reasonable values), is that one may obtain the Doppler-shifting current for the coordinate pair $k - \omega$ corresponding to the peak in the wavenumber–frequency spectrum. Once the current magnitude has been obtained, an important step is to find the depth at which that current lies, that is, relate the current felt by a particular wave directly to the water velocity at some depth. In years past, research in the field of radar remote sensing provided for the interpretation of this difference

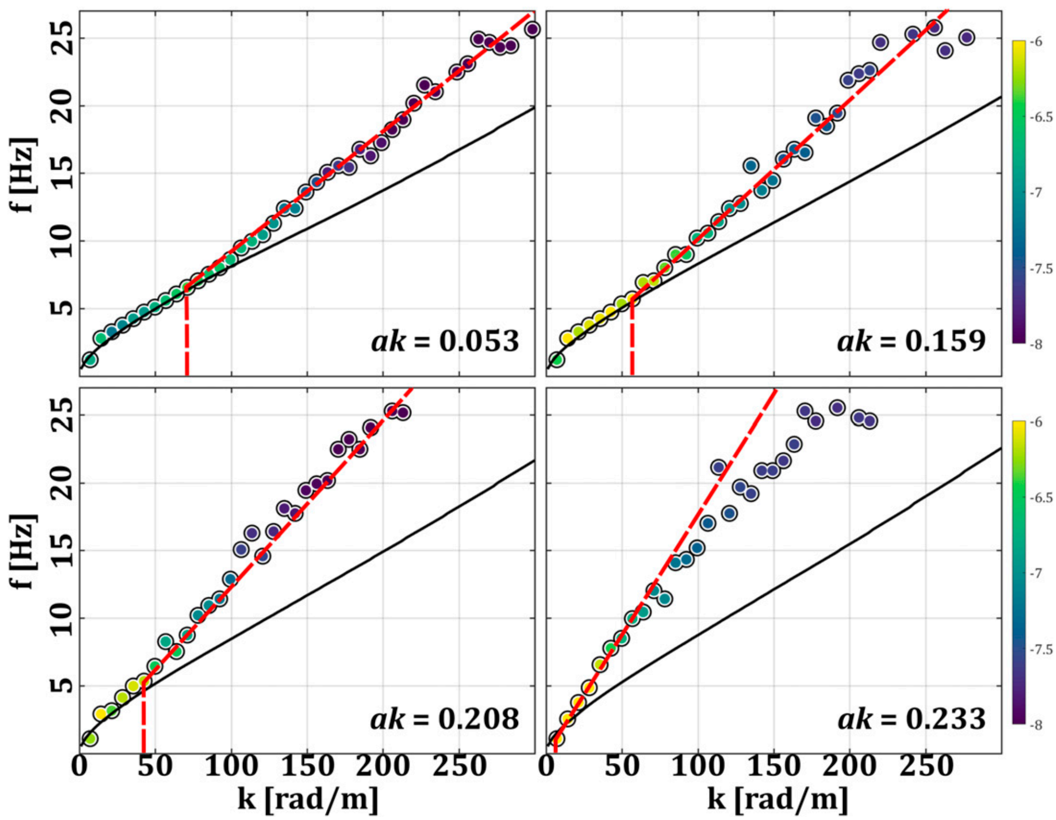

FIG. 3. Example wavenumber–frequency spectra. The color bar indicates the base-10 logarithm of unidirectional slope spectral energy density (m). For all four cases, $u_* = 0.161\ \mathrm{m\,s^{-1}}$, with long-wave paddle steepness given in each panel. The black line indicates the linear dispersion relation in the presence of the true currents observed by camera tracking of dye. The red dashed lines vertically represent the position of the dominant wave and then slope off on the figure as $c_p/2\pi = f/k$. These positions define the high cutoff wavenumber (c_p) used in the application of these spectra toward current retrieval: 71.0 rad $\mathrm{m^{-1}}$ (0.61 $\mathrm{m\,s^{-1}}$), 57.2 rad $\mathrm{m^{-1}}$ (0.64 $\mathrm{m\,s^{-1}}$), 42.5 rad $\mathrm{m^{-1}}$ (0.79 $\mathrm{m\,s^{-1}}$), and 7.0 rad $\mathrm{m^{-1}}$ (1.03 $\mathrm{m\,s^{-1}}$), in order of increasing paddle frequency.

between observed short-wave celerity and short-wave celerity from linear wave theory as the current at some decimal multiple of the wavelength [e.g., $c_p - c_0 = U(-0.080\lambda)$ (Stewart and Joy 1974) and $c_p - c_0 = U(-0.044\lambda)$ (Plant and Wright 1980)]. The capability afforded by wavenumber–frequency analysis of short-wave fields allows for this interpretation to be carried out simultaneously at multiple wave scales, resulting in the recovery of multiple current components at multiple depths.

The current of encounter estimated via this method is quasi-Lagrangian—a wave-scale-based portion of the overall Lagrangian current. That is, the Doppler shift felt by a particular wave component is representative of the (Eulerian) background current, the (Eulerian) wind drift, and a portion of the (Lagrangian) Stokes drift—all acting over the wave component's penetration depth (Young et al. 1985). The relevant portion of the Stokes drift is the net (i.e., time averaged) effect on the component in question by advection via orbital motions of waves that are sufficiently large in scale. As an example, it is reasonable to expect a 5-cm wave to be advected by a 50-cm wave but not by a 5.1-cm wave (and certainly not by a 4.9-cm wave). This topic of scale separation in Stokes drift and short-wave advection is beyond the scope of this paper; the method, however, may offer the capability for tackling such a problem in the future.

c. Bound waves: Waves advected by waves

Gravity–capillary waves on the water surface also respond hydrodynamically to the dominant wave scale via modulation and advection (e.g., Keller and Wright 1975; Plant 1989; Laxague et al. 2017). Under certain circumstances, the higher-wavenumber portion of the wave field may become bound to the dominant wave, traveling at its celerity (Plant et al. 1999b). Bound waves have been found to occupy a great share of the gravity–capillary and capillary waves generated in wind-wave

TABLE 1. Laboratory experimental conditions.

U_{10} (m s^{-1})	u_* (m s^{-1})	Paddle wave steepness ak (rad)	Paddle wave amplitude a (m)
4.99	0.161	0	0
5.63	0.183	0	0
6.26	0.207	0	0
6.90	0.231	0	0
7.53	0.257	0	0
8.17	0.283	0	0
4.99	0.161	0.053	0.009
4.99	0.161	0.159	0.026
4.99[a]	0.161[a]	0.208[a]	0.034[a]
4.99[a]	0.161[a]	0.233[a]	0.038[a]
8.17	0.283	0.086	0.014
8.17	0.283	0.106	0.017

[a] Case of higher paddle wave amplitude.

tanks—especially at conditions of low wind speed and high dominant wave amplitude (Plant et al. 1999b). The reaction of the high-wavenumber tail of the spectrum to a long wave is shown in Fig. 3. All four cases have the same wind forcing condition and the paddle wavenumber $k_{\text{paddle}} = 6.2\,\text{rad}\,\text{m}^{-1}$, with the paddle wave amplitude increasing from upper left to upper right to lower left to lower right. The wavenumber–frequency spectra of Fig. 3 provide strong evidence that simply increasing the amplitude of the paddle-generated wave changes the dominant short wind-sea peak wavenumber, altering the wave scale to which shorter waves will be bound. This is seen in Fig. 3, as short-wave celerity increases with paddle wave amplitude relative to the modified dispersion relation we would expect to arise due to pure advection by current. The red dashed lines show that waves shorter than the wind-sea peak are bound in celerity to the dominant wave.

Based on examination of these spectra, it is evident that the wavenumber position of the wind-sea peak limits the scale at which the analysis described in section 2b may be performed. However, following the interpretation of Stewart and Joy (1974) and Plant and Wright (1980), we may still obtain very near-interface current measurements from the polarimetric wavenumber–frequency spectra without using the high-wavenumber tail that is contaminated by bound waves. The domain over which short waves may be interpreted as being advected by currents (and not by the dominant wave) is shown in Fig. 3 as the interval between $k = k_{\min}$ and the red dashed line. This cutoff wavenumber is the position of the peak

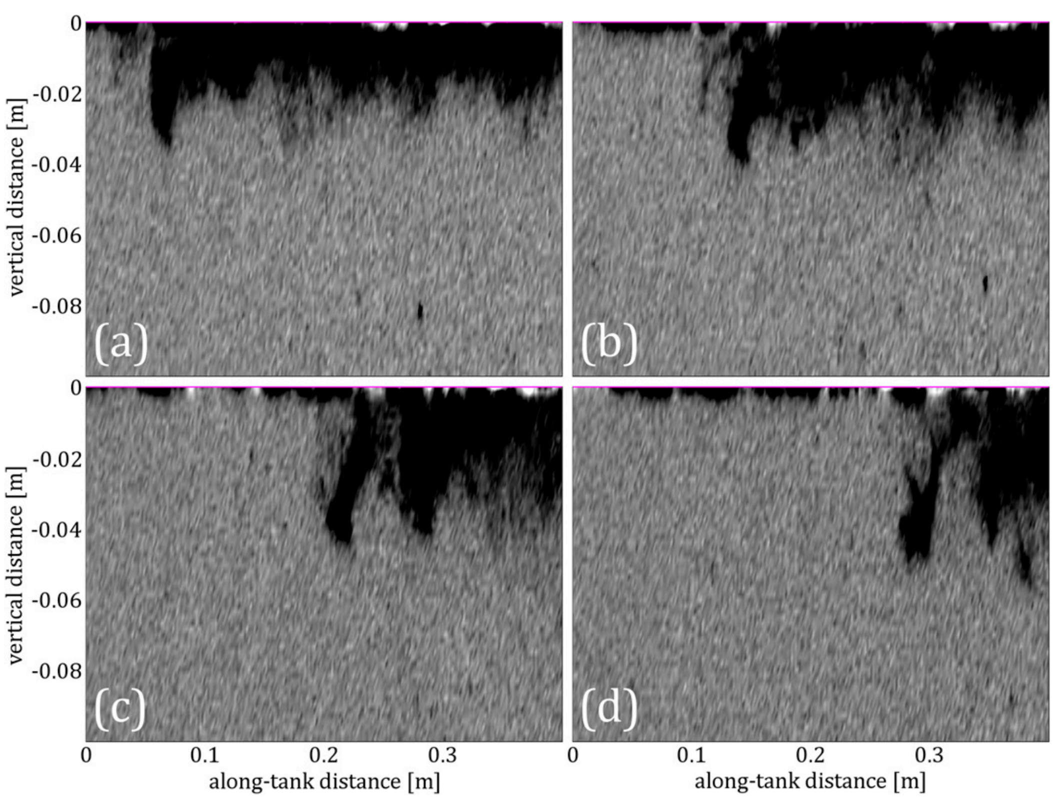

FIG. 4. (a)–(d) Four sequential high-contrast intensity fields of dye position, *only* water pump and fan. Image separation time is 1 s. The magenta line indicates the mean location of the interface.

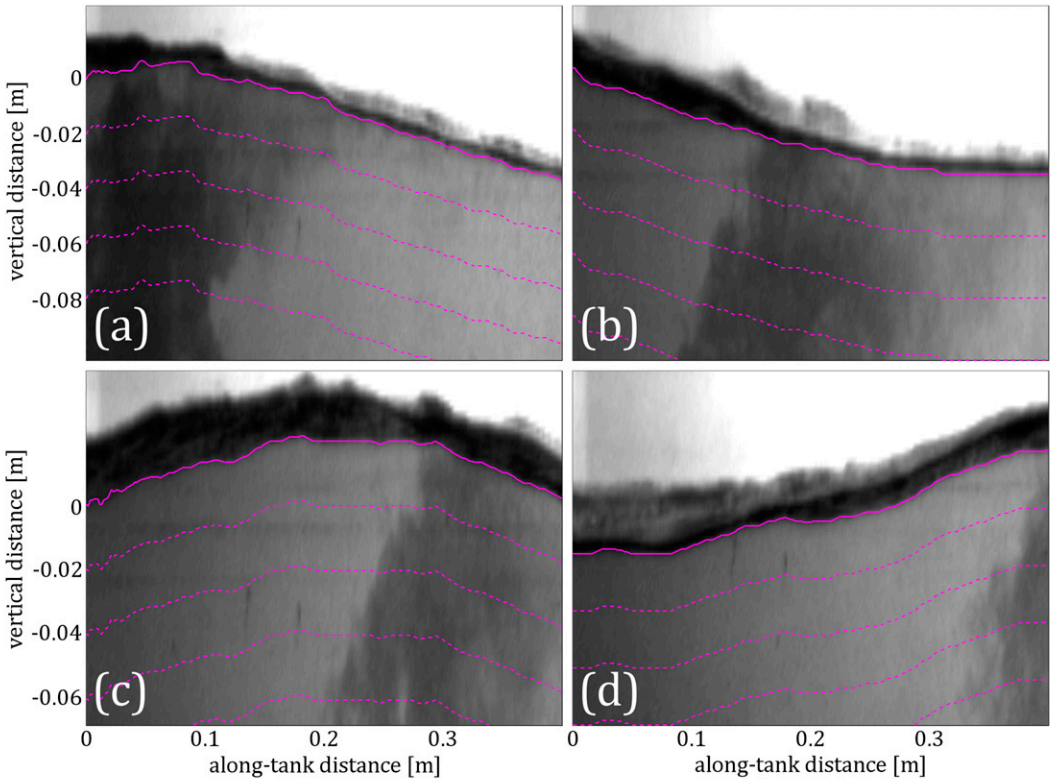

FIG. 5. (a)–(d) Four sequential high-contrast intensity fields of dye position. Image separation time is 1s. The solid magenta line indicates the instantaneous location of the interface. Dashed magenta lines indicate isobaths separated by 0.02 m.

energy density in the slope spectrum along the principal wave propagation direction: waves shorter than the dominant wave propagate lockstep together, while waves longer than the dominant wave are not bound thusly. It should be noted that the presence of long waves in the open ocean will not necessarily prevent retrieval of current in the field environment, as bound waves are far more common in wind-wave tanks than on the ocean surface (Plant 1997). Two case studies in which this method is applied outside of the laboratory are shown in section 3.

d. Supporting work

1) LABORATORY—WIND-WAVE TANK

For the laboratory validation studies, the wave slope and current retrieval methods described in section 2a were applied to polarimetric images acquired inside a wind-wave tank. In this setup, the camera tracking of dye was used to provide validation. Observations were performed in the Air-Sea Interaction Saltwater Tank (ASIST) at the University of Miami's Surge-Structure Atmosphere Interaction (SUSTAIN) facility. The acrylic tank extends 15 m, with a 1 m × 1 m cross-sectional area, and was filled with freshwater to a depth of 0.43 m. Wind forcing was measured via a sonic anemometer, with the sampling volume centered at 0.285 m above the mean water level. Observations were made at six different wind speeds, with u_* ranging from 0.161 to 0.283 m s^{-1}. For two wind forcing conditions ($u_* = 0.161$ m s^{-1} and $u_* = 0.283$ m s^{-1}), gravity waves of wavenumber $k = 6.2$ rad m^{-1} were generated by the hydraulic paddle and propagated through the flume. This information is also provided in Table 1. Note that the two cases of higher paddle wave amplitude (indicated by a footnote in the table; also shown as the bottom two panels in Fig. 3) are not used for current retrieval due to the paucity of data between $k_{\min}$ and k_{cutoff}. For all cases, a background current of 0.12 m s^{-1} was pumped through the volume to counteract the effects of any bottom-following flow that might be induced by the returning wind-induced current. The polarimetric camera was positioned 2.47 m above the tank's water level and oriented at 45° below the horizontal, providing for a pixel size of 1.0×10^{-3} m and rectified image dimensions of 0.78 m × 0.78 m, with the frame centered at 5-m fetch. Spectrally, this set a wavenumber range of 7.1–2771.8 rad m^{-1}. However,

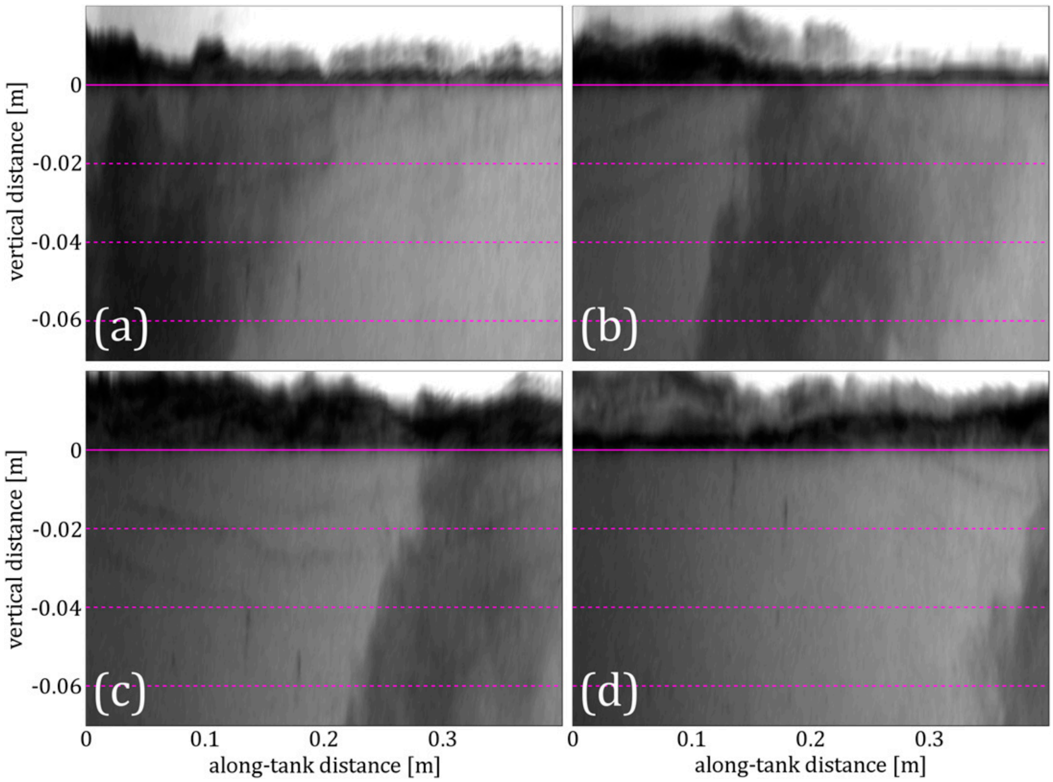

FIG. 6. As in Fig. 5, but adjusted into interface-following reference frame.

the presence of bound waves (section 2c) prevented consideration of the spectrum at wavenumbers above that of the short-wave peak (generally no higher than $100\,\mathrm{rad\,m^{-1}}$).

Complementary current measurements were made via the camera tracking of dye. In this setup, a Basler Ace (piA1000-60 gm) camera was fitted with a 12-mm focal length lens (configured to minimize lens distortion) and oriented to face the side of the tank. The far side of the sampling volume was lit by an along-tank array of 1000-W halogen lamps in order to provide uniform illumination.

The first part of these observations involved tracking the rapidly moving dye that rests in the upper $\approx$0.001 m of the water. The second part of these observations involved the tracking of the edge of an injected dye plume, estimating the drift profile in the upper 0.1 m. The dark portions of Fig. 4 represent water with a high concentration of dye. The speckled gray portions represent the uncolored background water. The position of the trailing edge of the dye plume was tracked for each frame, ultimately yielding an along-tank current magnitude for a single dye injection. The trailing edge was chosen in order to maximize the image intensity gradient; molecular diffusion of dye occurred strongly along the leading boundary but was suppressed along the trailing boundary by the flow, resulting in a sharp distinction on that edge. This observation was repeated over five trials for each condition to obtain a mean profile on $z = (-0.1, -0.005)$ m. The same analysis was performed for conditions with paddle-generated waves (Fig. 5). For these conditions, current estimates were made after the images had been transformed into a long-wave interface-following reference frame (Fig. 6).

2) FIELD—MOUTH OF THE COLUMBIA RIVER

For the field portion of this study, observations were made in the MCR along the Oregon–Washington border in June of 2013. The MCR is a reinforced macrotidal inlet with strong (sometimes close to $2\,\mathrm{m\,s^{-1}}$) ebb currents, swells incident from the west-northwest, and highly variable wind forcing conditions. These measurements were made as part of the second Office of Naval Research–sponsored Riverine and Estuarine Transport (RIVET-II) experiment. A large-scale goal of this multipronged campaign was to provide in situ observations of coastal wave–current–wind interaction that would benefit the future use of remote sensing platforms for sampling these dynamic regions. Drawing connections between atmospheric forcing, wave

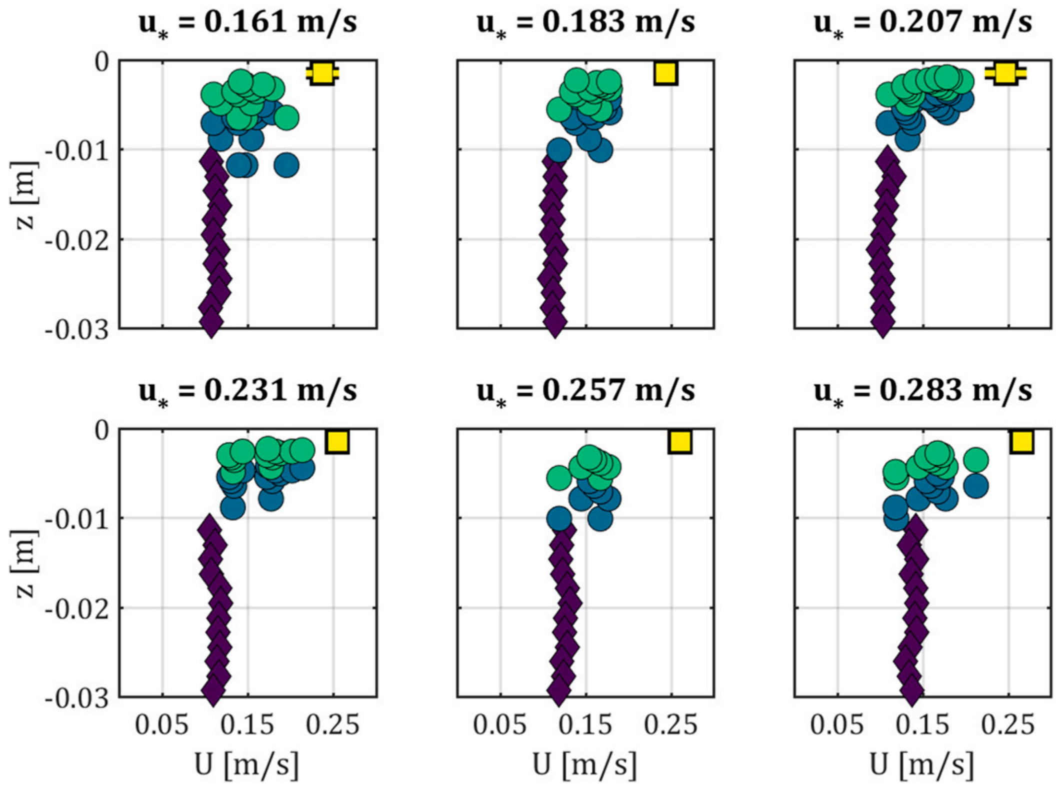

FIG. 7. Current profiles without paddle waves. Violet diamonds represent camera-tracked dye speeds beneath the surface, and the yellow square represents the camera-tracked dye speed at the surface. Blue and green circles represent Δc_p as inferred from the $k-\omega$ spectra obtained via polarimetry, with the depth of the blue circles computed as $c_p - c_0 = U(-0.080\lambda)$ (Stewart and Joy 1974) and the depth of the green circles computed as $c_p - c_0 = U(-0.044\lambda)$ (Plant and Wright 1980). Recall that the maximum depth for each profile is set by the imaging field of view.

conditions, and remotely sensible parameters were therefore a high priority of the campaign. Application of established open-ocean-style wind, wave, and current measurements were made in the highly energetic environment of the MCR. The R/V *Point Sur* served as host to the wave and wind sensor suite, allowing for the observation of wind forcing, long-wave behavior, and short-wave spatial structure from a moving or quasi-stationary frame of reference.

A sonic anemometer was fastened atop a meteorological mast mounted on the prow (2.3 m above the deck), providing three-dimensional wind velocities 8.1 m above the mean sea level. The vessel's angular and linear accelerations were logged at 10 Hz via a Systron Donner 6-degrees-of-freedom motion package, which was located adjacent to the sensor suite on the ship's bow. This was used to motion correct the flux measurements and to properly rectify the polarimeter frames. Simultaneous measurements of vessel motion enabled the 10-Hz winds measured from the sonic anemometer to be corrected for the vessel accelerations and translation Anctil et al. (1994). The total stress vector on the water surface was estimated by computing the covariance of the turbulent along- and across-wind velocities (u' and v', respectively) with the vertical wind component w',

$$\boldsymbol{\tau}_{\text{wind}} = -\rho_{\text{air}}[\langle u'w'\rangle\hat{x} + \langle v'w'\rangle\hat{y}], \tag{11}$$

where ρ_{air} is the air density and a prime indicates a turbulent quantity in a Reynolds decomposition (i.e., $\langle u'\rangle = \langle v'\rangle = \langle w'\rangle = 0$). The angle brackets indicate that a time average of the contained quantity has been computed over an interval—here, 5 min. This averaging window was used to balance the satisfactory retrieval of spatial roughness variability with vessel translation, following similar work done by Ortiz-Suslow et al. (2015) at a different tidal inlet. The relatively short window was required on account of the high spatial variability in bathymetry, currents, and surface interactions in this coastal zone. The U_{10} reported in this work is the 10-m neutral wind speed calculated using the eddy-covariance techniques, while the wind stress τ comes directly from the along- and across-wind covariance components of the Reynolds stress [Eq. (11)].

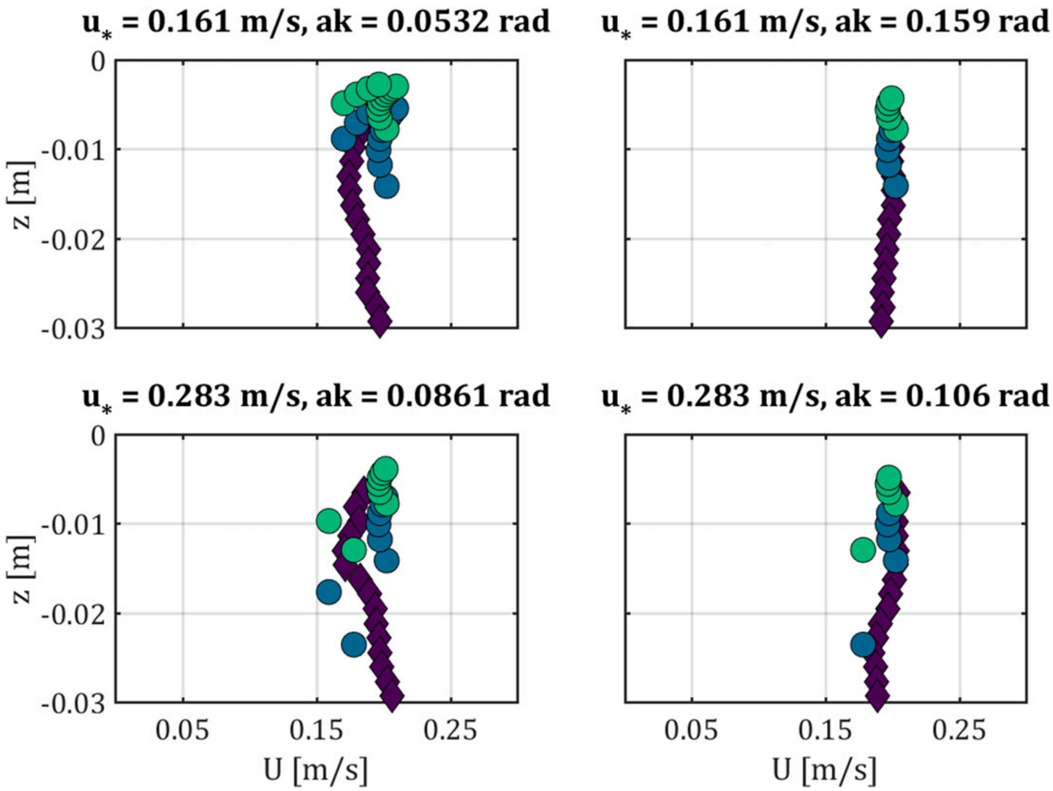

FIG. 8. Current profiles with paddle waves. Violet diamonds represent camera-tracked dye speeds beneath the surface. Blue and green circles represent Δc_p as inferred from the $k-\omega$ spectra obtained via polarimetry, with the depth of the blue circles computed as $c_p - c_0 = U(-0.080\lambda)$ (Stewart and Joy 1974) and the depth of the green circles computed as $c_p - c_0 = U(-0.044\lambda)$ (Plant and Wright 1980).

Water surface elevation was obtained from a triplet of ultrasonic distance meters (UDMs), mounted forward such that their elevation measurements were not contaminated by the ship's wake zone. For both field cases considered, the ship's rotational motion was negligible. The elevation observations were corrected via rotation into the earth reference frame using the simultaneously sampled linear accelerations and rotation rates. Once this operation had been performed, the corrected water surface elevation time series were processed using the iterated maximum likelihood method (IMLM) of Pawka et al. (1984), producing a frequency–direction elevation variance spectrum (m^2 Hz^{-1} deg^{-1}). This method of directional wave spectrum determination is computationally efficient and was well suited to the relatively mild wave conditions (H_s = 0.21, 0.39 m, respectively) at the measurement locations inside the jetties (Benoît 1993).

3. Results

The first results presented are those from the laboratory measurements. The analysis performed here takes advantage of celerities from waves with wavenumbers lower than the wind-sea peak, with depth assignment given as some multiple of wavelength (provided in the figure captions). Six cases are shown using data collected during ''wind only'' conditions (Fig. 7), with profile and surface dye speed given along with the currents estimated via wavenumber–frequency analysis of the polarimetric slope fields. Horizontal error bars on the surface dye estimates indicate 95% confidence intervals. The four cases (Fig. 8) include the two lowest-steepness paddle conditions. The two highest-steepness paddle conditions pushed the peak of the wavenumber spectrum to the edge of spectral domain, essentially binding all observed waves to the dominant celerity (as described in section 2c).

For the chosen field cases, the wind velocity vector was oriented (''going to'' convention) in the vicinity of north (MCR-1) and northwest (MCR-2). Supporting current data were supplied by a moored USGS 1200-kHz ADCP. The moored current meter was not exactly collocated with the shipboard observations (Fig. 9); however, it provided useful information, namely, current observations closer to the air–sea interface than the >6-m-deep measurements given by the shipboard ADCP.

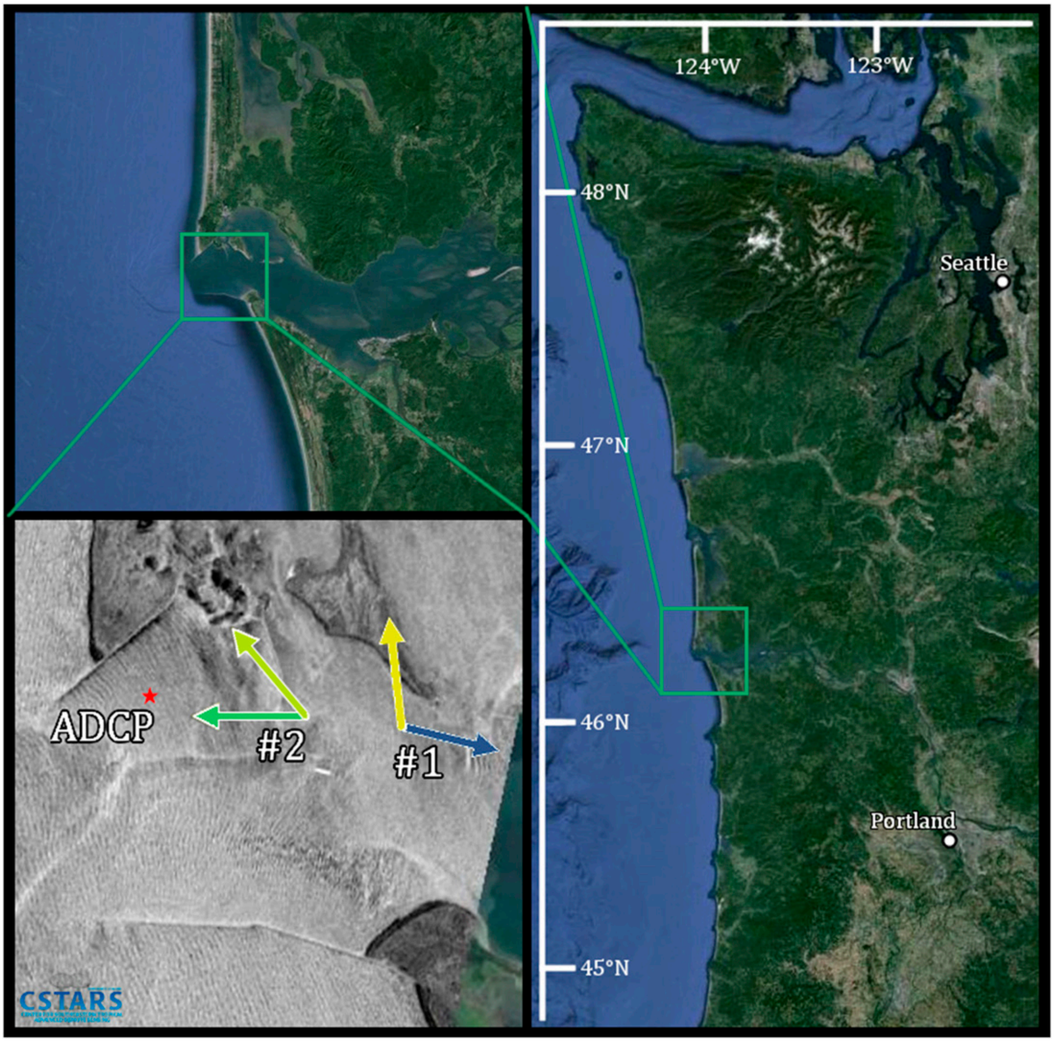

FIG. 9. From large to small scale: (right) Pacific Northwest, (top left) wide view of MCR, and (bottom left) tight view of the river inlet. In the bottom-left panel, the smallest frame with overlaid *TerraSAR-X* intensity data collected near the time of MCR-1. For reference, the ship's position at each case is given as the vertex of a pair of colored arrows (of arbitrary length, scaled for aesthetics). For MCR-1, the yellow arrow indicates the absolute wind stress direction as measured from the R/V *Point Sur* (≈351°) and the blue arrow indicates the tidal current direction as measured by shipboard ADCP (≈110°). For MCR-2, the lighter green arrow indicates the absolute wind stress direction (≈326°) and the darker green arrow indicates the tidal current direction (≈270°). The red star marks the location of the moored USGS ADCP.

For MCR-1, the R/V *Point Sur* lay just south of Sand Island inside the river mouth (Fig. 9). Five minutes of slope fields (ending with 1439:00 UTC 2 June 2013) were evaluated to produce a single wavenumber–frequency spectrum. In this situation, the short-wave direction and absolute wind stress direction (i.e., wind direction plus/minus the stress angle) were aligned at ≈350°, while the long-wave direction (Fig. 10) was oriented at ≈20°. The river mouth was experiencing a flooding tide, with the ocean water running into the river mouth at ≈100°. These relative directions are shown overlaid on a Synthetic Aperture Radar (SAR) intensity image from the *TerraSAR-X* satellite that was collected at the time of measurement in Fig. 9, with the moored ADCP location given as a red star. The currents from this period are shown in Fig. 11, where color represents degrees clockwise from north. The ADCP profile and polarimetry profile show a strongly sheared environment, with a stark divergence of the near-surface wind-driven current from the background tidal flow. Specifically, the surface drift has approximately twice the magnitude of the middepth flow (as measured by ADCP), with a directional separation of ≈110° between the two.

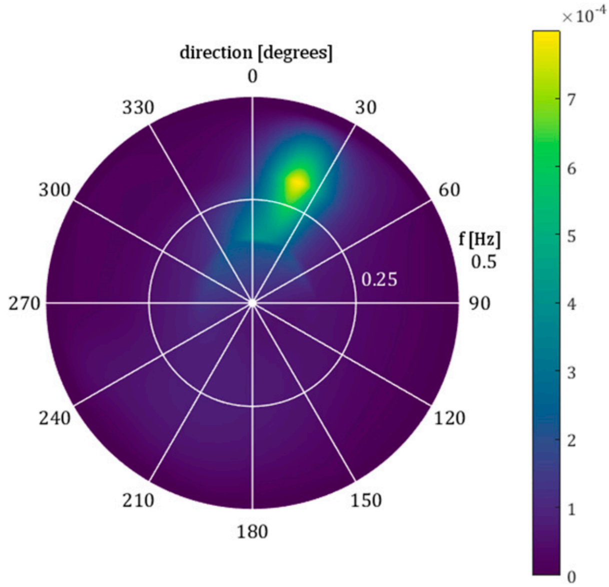

FIG. 10. Directional long-wave spectrum for MCR-1, as determined from shipboard ultrasonic distance meter UDM array: $H_s = 0.21$ m, $T_p = 3.24$ s, peak wave direction = 355°. Color bar indicates water surface elevation spectral density (m^2 Hz^{-1} deg^{-1}). Wind velocity direction: 12.74°, wind velocity magnitude: 9.14 m s^{-1}; wind stress direction: 351.85°, wind stress magnitude: 0.0508 N m^{-2}.

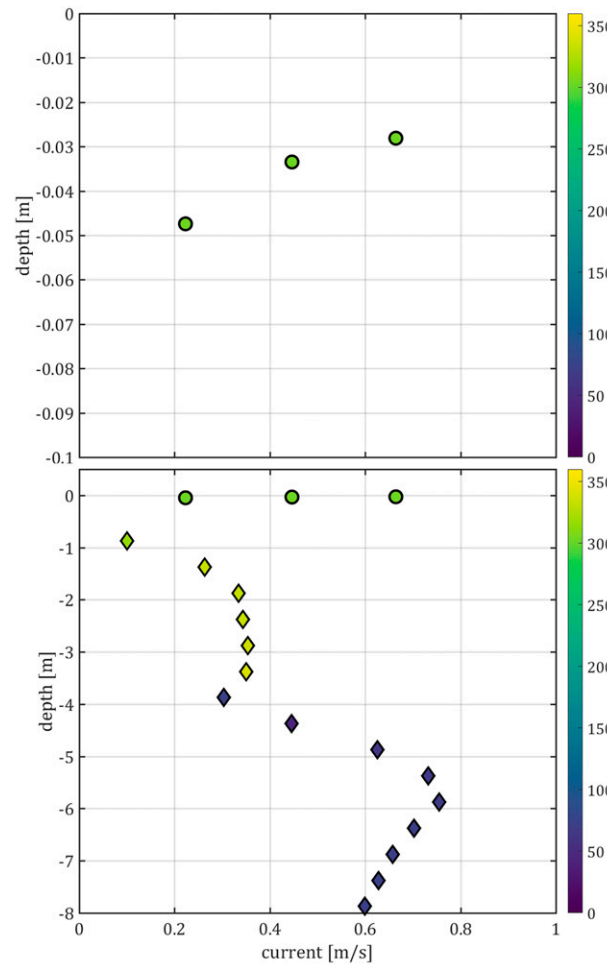

FIG. 11. The time-averaged current profile for MCR-1. (bottom) Full derived profile and (top) an expansion of the upper 0.1 m of the profile. Data presented include current observations from the polarimetric wave slope sensing method (●) and the moored ADCP (◆). Each symbol's fill color corresponds to its direction (deg) clockwise from true north in an oceanographic going-to convention. Wind velocity direction: 12.74°, wind velocity magnitude: 9.14 m s^{-1}; wind stress direction: 351.85°, wind stress magnitude: 0.0508 N m^{-2}.

For MCR-2, the ship's position was slightly to the west of the previous location, though still in the river mouth. Data for this case was taken from the approximately 1-min period ending with 1349:56 UTC 7 June 2013. In this instance, the long-wave direction (Fig. 12) was observed to be at ≈100°, while the short-wave direction and wind stress direction were aligned at ≈325°. In this case, the river mouth was experiencing a strong ebbing tide, with the river water exiting the mouth at ≈270°. The currents from this period are shown in Fig. 13, where color represents degrees clockwise from north. In this situation, the surface drift is actually weaker than the tidal current at depth. Trusting in the magnitude of the nearest-surface ADCP observations seems more reasonable in this situation, as the wave conditions ($T_p = 6.2$ s, $\lambda_p = 60.4$ m, $ak = 0.02$ rad) are much more amenable to the use of current profilers.

4. Discussion

For the laboratory observations, the current profiles retrieved by the spectral analysis methods presented in this work occupy the space between the surface and centimeter-depth dye-tracked current speeds. For the paddle wave conditions (Fig. 8), the curved shape of the spectrally obtained current profiles is mirrored by the shape of the dye profiles, indicating that the methods presented here implicitly retrieve current profiles in an interface-following reference frame. The depth assignment of Stewart and Joy (1974) provides a near-surface profile that is especially close to the dye observations, directly describing the shear between the centimeter-depth flows and the rapid surface (millimeter depth) drift. Furthermore, the thickness of this layer is consistent with the approximate thickness of the viscous sublayer for the wind conditions used here (Wu 1971), indicating that the values of Δc_p retrieved via the methods presented here are indeed representative of currents at the depths given by Stewart and Joy (1974) and Plant and Wright (1980).

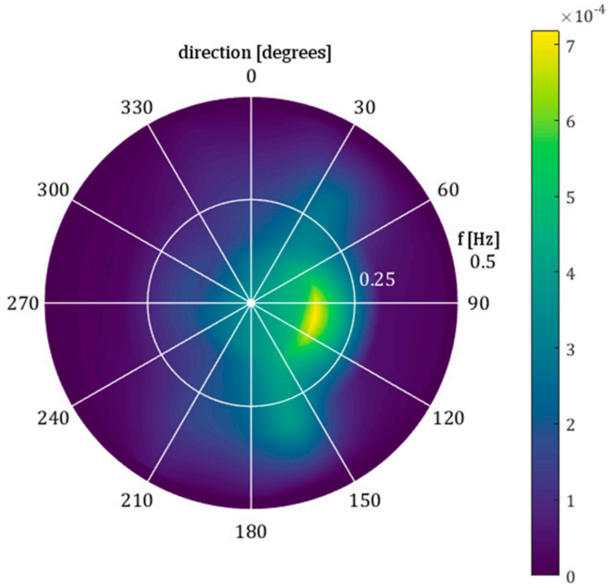

FIG. 12. Directional long-wave spectrum for MCR-2, as determined from shipboard UDM array: $H_s = 0.39$ m, $T_p = 6.22$ s, peak wave direction = 270°. Color bar indicates water surface elevation spectral density (m^2 Hz^{-1} deg^{-1}). Wind velocity direction: 321.48°, wind velocity magnitude: 10.99 m s^{-1}; wind stress direction: 326.72°, wind stress magnitude: 0.0175 N m^{-2}.

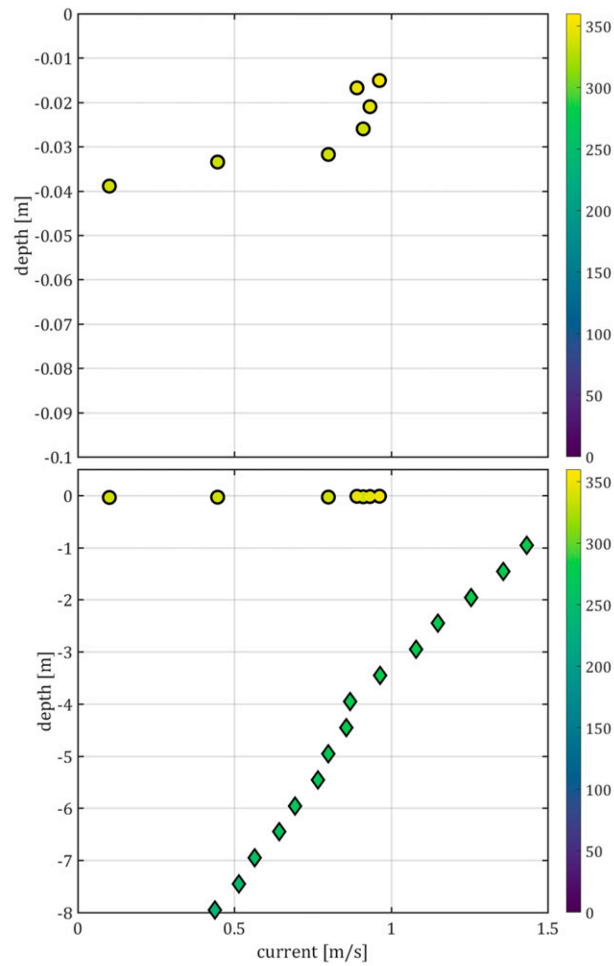

FIG. 13. The time-averaged current profile for MCR-2. (bottom) Full derived profile and (top) an expansion of the upper 0.1 m of the profile. Data presented include current observations from the polarimetric wave slope sensing method (●) and the moored ADCP (◆). Each symbol's fill color corresponds to its direction (deg) clockwise from true north in an oceanographic going-to convention. Wind velocity direction: 321.48°, wind velocity magnitude: 10.99 m s^{-1}; wind stress direction: 326.72°, wind stress magnitude: 0.0175 N m^{-2}.

In the field observations, there were no in-water current meters that could suitably observe the near-surface behavior of the current profile. Given the findings from the laboratory, the optical method was considered as a validated direct measurement of the current profile in the uppermost portion of the water column. However, the field environment brings challenges that the laboratory does not have with regard to observing near-interface currents with this method. Beyond ship motion, which was minimized by design during data collection, the two factors that differ most from the laboratory setting are the direction of the wind vector and the existence of long gravity waves. For the former, one is not able to make assumptions a priori about the direction of the surface drift; it must be inferred from the direction of dispersion shell shift. In both presented cases, however, the method was able to identify the wind stress direction to within 5° independently of a direct wind measurement. For the latter challenge, long waves present the issue of advection by orbital motions. Indeed, this contribution can be difficult to isolate given the ≈1-min averaging time used for this method. The focus here, then, has been to minimize the issue by selecting observational periods with slight long-wave presence. For both field cases, long-wave orbital motions were estimated via linear wave theory to reach a maximum of 0.20 m s^{-1} at the air–sea interface. While this is nonnegligible, it represents a maximum of 12.5% of the observed surface drift considering the 45°–90° difference between long-wave propagation and short-wave/surface drift directions. All of this is to say that while the method described in this work is far from universally applicable, it can be revealing if the conditions are appropriate.

In MCR-1, the large (≈110°) amount of veering with depth appears to be an alignment of the near-surface current with the wind stress and peak short-wave directions ($\theta_\tau \approx 350°$). Results from MCR-2 depict a situation in which the wind stress and short-wave directions are aligned at ≈325°, but the tidal current is oriented at ≈270°. The moored ADCP and decimeter-depth polarimetric current observations are nearly continuous in magnitude and direction.

Comparison of these cases is compelling evidence that near-surface [$z = -O(0.01)$ m] wind-induced currents may behave irrespective of the long-wave field, tidal currents at depth, or even free-stream wind direction, owing their motion instead to the physical stresses exerted on the water by the atmosphere, which can vary from the wind direction due to a variety of factors (Zhang et al. 2009; Ortiz-Suslow et al. 2015). It is quite important to note that although the wind speed for MCR-1 is less than that of MCR-2 (9.14 and 10.99 $\mathrm{m\,s^{-1}}$, respectively), the eddy-covariance wind stress magnitude for MCR-1 exceeds that of MCR-2 by nearly a factor of 3 (0.0508 and 0.0175 $\mathrm{N\,m^{-2}}$, respectively). A wind stress estimate derived from a wind speed–dependent bulk parameterization would have missed this subtlety. This connection between the near-surface current and the stress vector also has implications for the parameterization of oceanic surface drift. Specifically, the addition of 3.5% of U_{10} (or 0.55% of some bulk u_*) as surface drift in the wind velocity direction may not be appropriate when stress is of high magnitude or is steered by external forces.

5. Conclusions

A new application of Fourier analysis has been developed to observe very near-surface current profiles using a single-point passive imaging technique. The technique was tested in a wind-wave laboratory and its results agreed well with camera-tracked dye speeds. These corroborating observations have opened a door for the application of high-wavenumber, high-frequency spectral analysis to near-surface current retrieval. The strong agreement between our estimates of the nearest-surface current velocities and the dye motions is an especially good empirical indicator that $\mathbf{U}_E$ contains within it a great deal of the full Lagrangian velocity responsible for material transport. The technique produces accurate current magnitude and direction estimates that correspond to depths within centimeters of the undulating free surface without having to disturb any portion of the air–sea interface. The field observations indicated the complex nature of coastal, nearshore, and river mouth environments. Short ocean waves may or may not be explicitly governed by the wind velocity direction alone. Their apparent two-way coupling with the wind stress, however, is evident through these examples. This is manifested in both the direction of the wind-driven current and the magnitude of that current relative to cases with similar wind speed magnitude.

Near-surface currents are of critical importance in the estimation of oceanic material transport—especially transport of the ecologically damaging materials of spilled oil or marine debris. Based in part on the results presented here, future parameterizations of marine transport would be greatly aided by a consideration of the magnitude and direction of ocean–atmosphere momentum flux. Further extensions of this method into the field are being applied presently and include a variety of shipboard, airborne, and drifting instruments for a more thorough investigation of these small-scale dynamics. Ultimately, this new technique for passively optical, near-surface current profile determination offers previously unavailable information for the fields of physical remote sensing and near-interface fluid mechanics.

Acknowledgments. The authors thank two anonymous reviewers and Dr. Bill Plant for their guidance over the course of this work's development. This research was made possible in part by Grant SA1207-GOMRI005 from the Gulf of Mexico Research Initiative and in part by Grant N000141410643 from the Office of Naval Research. Data are publicly available through the Gulf of Mexico Research Initiative Information and Data Cooperative (GRIIDC; https://data.gulfresearchinitiative.org; doi:10.7266/N7KP805V). Thanks are given to all those who worked on and prepared for our portion of the RIVET-II experiment, in particular Neil Williams and Mike Rebozo. Thanks are also given to Andrew Stevens of the U.S. Geological Survey for providing the moored ADCP data used here. The authors are grateful to the captain and crew of the R/V *Point Sur* for their hard work and careful execution through conditions ranging from quiet to rough. A conversation nearly 3 years after the RIVET-II experiment between Milan Curcic, Jan-Victor Björkqvist, and Nathan Laxague proved to be exceptionally illuminating to the last individual and provided a great deal of important background to this work. Last but not least, the authors thank Eric Firing, Stéfan van der Walt, and Nathaniel Smith for the design and distribution of Viridis, the fairest colormap of them all.

REFERENCES

Anctil, F., M. A. Donelan, W. M. Drennan, and H. C. Graber, 1994: Eddy-correlation measurements of air-sea fluxes from a discus buoy. *J. Atmos. Oceanic Technol.*, **11**, 1144–1150, doi:10.1175/1520-0426(1994)011<1144:ECMOAS>2.0.CO;2.

Barrick, D. E., M. Evans, and B. Weber, 1977: Ocean surface currents mapped by radar. *Science*, **198**, 138–144, doi:10.1126/science.198.4313.138.

Benoît, M., 1993: Extensive comparison of directional wave analysis methods from gauge array data. *Ocean Wave Measurement and Analysis: Proceedings of the Second International Symposium*, American Society of Civil Engineers, 740–754.

Bock, E. J., and T. Hara, 1995: Optical measurements of capillary-gravity wave spectra using a scanning laser slope gauge.

J. Atmos. Oceanic Technol., **12**, 395–403, doi:10.1175/1520-0426(1995)012<0395:OMOCGW>2.0.CO;2.

Goldstein, R., H. Zebker, and T. Barnett, 1989: Remote sensing of ocean currents. *Science*, **246**, 1282–1285, doi:10.1126/science.246.4935.1282.

Hara, T., E. J. Bock, and D. Lyzenga, 1994: In situ measurements of capillary-gravity wave spectra using a scanning laser slope gauge and microwave radars. *J. Geophys. Res.*, **99**, 12 593–12 602, doi:10.1029/94JC00531.

Harkins, W. D., and F. Brown, 1919: The determination of surface tension (free surface energy), and the weight of falling drops: The surface tension of water and benzene by the capillary height method. *J. Amer. Chem. Soc.*, **41**, 499–524, doi:10.1021/ja01461a003.

Hasselmann, K., and M. Schieler, 1970: Radar back-scatter from the sea surface. *Eighth Symposium on Hydrodynamics: Hydrodynamics in the Ocean Environment*, M. S. Plesset, T. Y.-T. Wu, and S. W. Doroff, Eds., ARC-179, Office of Naval Research, 361–388.

Keller, W., and J. Wright, 1975: Microwave scattering and the straining of wind-generated waves. *Radio Sci.*, **10**, 139–147, doi:10.1029/RS010i002p00139.

Laxague, N. J., B. K. Haus, D. Bogucki, and T. Özgökmen, 2015: Spectral characterization of fine-scale wind waves using shipboard optical polarimetry. *J. Geophys. Res. Oceans*, **120**, 3140–3156, doi:10.1002/2014JC010403.

——, D. G. Ortiz-Suslow, B. K. Haus, N. J. Williams, and H. C. Graber, 2016: Water surface slope spectra in nearshore and river mouth environments. *IOP Conf. Ser.: Earth Environ. Sci.*, **35**, 012013, doi:10.1088/1755-1315/35/1/012013.

——, M. Curcic, J.-V. Björkqvist, and B. K. Haus, 2017: Gravity-capillary wave spectral modulation by gravity waves. *IEEE Trans. Geosci. Remote Sens.*, **55**, 2477–2485, doi:10.1109/TGRS.2016.2645539.

Leckler, F., F. Ardhuin, C. Peureux, A. Benetazzo, F. Bergamasco, and V. Dulov, 2015: Analysis and interpretation of frequency–wavenumber spectra of young wind waves. *J. Phys. Oceanogr.*, **45**, 2484–2496, doi:10.1175/JPO-D-14-0237.1.

Millard, R., and G. Seaver, 1990: An index of refraction algorithm for seawater over temperature, pressure, salinity, density, and wavelength. *Deep-Sea Res.*, **37A**, 1909–1926, doi:10.1016/0198-0149(90)90086-B.

Millero, F. J., and A. Poisson, 1981: International one-atmosphere equation of state of seawater. *Deep-Sea Res.*, **28A**, 625–629, doi:10.1016/0198-0149(81)90122-9.

Ortiz-Suslow, D., B. Haus, N. Williams, N. Laxague, A. Reniers, and H. Graber, 2015: The spatial-temporal variability of air-sea momentum fluxes observed at a tidal inlet. *J. Geophys. Res. Oceans*, **120**, 660–676, doi:10.1002/2014JC010412.

Pawka, S., D. Inman, and R. Guza, 1984: Island sheltering of surface gravity waves: Model and experiment. *Cont. Shelf Res.*, **3**, 35–53, doi:10.1016/0278-4343(84)90042-6.

Plant, W. J., 1989: The modulation transfer function: Concept and applications. *Radar Scattering from Modulated Wind Waves: Proceedings of the Workshop on Modulation of Short Wind Waves in the Gravity-Capillary Range by Non-Uniform Currents*, G. J. Komen and W. A. Oost, Eds., Springer, 155–172.

——, 1997: A model for microwave Doppler sea return at high incidence angles: Bragg scattering from bound, tilted waves. *J. Geophys. Res.*, **102**, 21 131–21 146, doi:10.1029/97JC01225.

——, and J. Wright, 1980: Phase speeds of upwind and downwind traveling short gravity waves. *J. Geophys. Res.*, **85**, 3304–3310, doi:10.1029/JC085iC06p03304.

——, P. H. Dahl, and W. C. Keller, 1999a: Microwave and acoustic scattering from parasitic capillary waves. *J. Geophys. Res.*, **104**, 25 853–25 866, doi:10.1029/1999JC900168.

——, W. C. Keller, V. Hesany, T. Hara, E. Bock, and M. A. Donelan, 1999b: Bound waves and Bragg scattering in a wind-wave tank. *J. Geophys. Res.*, **104**, 3243–3263, doi:10.1029/1998JC900061.

Reed, M., C. Turner, and A. Odulo, 1994: The role of wind and emulsification in modelling oil spill and surface drifter trajectories. *Spill Sci. Technol. Bull.*, **1**, 143–157, doi:10.1016/1353-2561(94)90022-1.

Senet, C. M., J. Seemann, and F. Ziemer, 2001: The near-surface current velocity determined from image sequences of the sea surface. *IEEE Trans. Geosci. Remote Sens.*, **39**, 492–505, doi:10.1109/36.911108.

Stewart, R. H., and J. W. Joy, 1974: HF radio measurements of surface currents. *Deep-Sea Res. Oceanogr. Abstr.*, **21**, 1039–1049, doi:10.1016/0011-7471(74)90066-7.

Wu, J., 1971: An estimation of oceanic thermal-sublayer thickness. *J. Phys. Oceanogr.*, **1**, 284–286, doi:10.1175/1520-0485(1971)001<0284:AEOOTS>2.0.CO;2.

——, 1975: Wind-induced drift currents. *J. Fluid Mech.*, **68**, 49–70, doi:10.1017/S0022112075000687.

Young, I. R., W. Rosenthal, and F. Ziemer, 1985: A three-dimensional analysis of marine radar images for the determination of ocean wave directionality and surface currents. *J. Geophys. Res.*, **90**, 1049–1059, doi:10.1029/JC090iC01p01049.

Zappa, C. J., M. L. Banner, H. Schultz, A. Corrada-Emmanuel, L. B. Wolff, and J. Yalcin, 2008: Retrieval of short ocean wave slope using polarimetric imaging. *Meas. Sci. Technol.*, **19**, 055503, doi:10.1088/0957-0233/19/5/055503.

——, ——, ——, J. R. Gemmrich, R. P. Morison, D. A. LeBel, and T. Dickey, 2012: An overview of sea state conditions and air-sea fluxes during RaDyO. *J. Geophys. Res.*, **117**, C00H19, doi:10.1029/2011JC007336.

Zhang, F. W., W. M. Drennan, B. K. Haus, and H. C. Graber, 2009: On wind-wave-current interactions during the Shoaling Waves Experiment. *J. Geophys. Res.*, **114**, C01018, doi:10.1029/2008JC004998.